Electronic Supplementary Material (ESI) for Journal of Materials Chemistry A.

Supporting Information

Enhanced localized electron density from PdCu nanoparticles loading on defective TiO_2 support for selective nitrate electroreduction to ammonia

Haoran Wu[a], Heng Guo[a,b,*], Fengying Zhang[a,b], Peng Yang[a] , Jiaxin Liu[a], Yuantao Yang[a], Zhen-Feng Huang[c], Chenyuan Zhu[d], Weitao Wang[d], Xin Tu[d,*], Guidong Yang[e], Ying Zhou[a,b,*]

[a] State Key Laboratory of Oil and Gas Reservoir Geology and Exploitation, Southwest Petroleum University, Chengdu, 610500, China

[b] School of New Energy and Materials, Southwest Petroleum University, Chengdu, 610500, China

E-mail: heng.guo@swpu.edu.cn, yzhou@swpu.edu.cn

Fax: +86 28 83037406; Tel: +86 28 83037411

[c] Key Laboratory for Green Chemical Technology of Ministry of Education, Collaborative Innovation Centre of Chemical Science and Engineering, School of Chemical Engineering and Technology, Tianjin University, Tianjin 300072, PR China

[d] Department of Electrical Engineering and Electronics, University of Liverpool, Liverpool L69 3GJ, United Kingdom

E-mail: xin.tu@liv.ac.uk

[e] XJTU-Oxford Joint International Research Laboratory of Catalysis, School of Chemical Engineering and Technology, Xi'an Jiaotong University, Xi'an, 7010049, China

*Corresponding authors: Heng Guo (heng.guo@swpu.edu.cn); Xin Tu (xin.tu@liv.ac.uk); Ying Zhou (yzhou@swpu.edu.cn)

Experimental Section

1. Materials

Titanium dioxide (TiO_2, 99.8% metals basis, 30 nm, anatase), Salicylic acid ($C_7H_6O_3$, AR), Sodium citrate tribasic dihydrate ($C_6H_5Na_3O_7 \cdot H_2O$, AR), Sodium hypochlorite solution (NaClO, AR), Palladium chloride ($PdCl_2$, 99.999% metals basis), Nafion117 solution (5 wt%) and Sodium nitrate -15N ($Na^{15}NO_3$, 99 atom%) were purchased from Aladdin Reagent Corp. Sodium borohydride ($NaBH_4$, AR), Sodium hydroxide (NaOH, GR), Copper chloride dihydrate ($CuCl_2 \cdot 2H_2O$, AR), Sodium sulfate (Na_2SO_4, AR), Sodium nitrate ($NaNO_3$, AR), Isopropyl alcohol (C_3H_8O, GR), and Ethanol (C_2H_6O, GR) were purchased from Chengdu Kelong Chemical Reagent Corp. Sodium nitroprusside ($C_5H_4FeN_6Na_2O_3$, 99.98% metals basis), and PVP ($(C_6H_9NO)_n$, average mol wt 10,000) were purchased from Sigma-Aldrich. Ar (99.999%) and H_2 (10%) were provided by Chengdu Keyuan Gas Corp. Ultrapure water (Millipore Milli-Q grade, 18.25 MΩ) was used in all experiments.

2. Preparation of defective TiO_{2-x}

The commercially available TiO_2 was used as the precursor to prepare oxygen vacancy-enriched TiO_{2-x} through a facile reduction method using $NaBH_4$. First, 200 mg TiO_2 and $NaBH_4$ were mixed thoroughly and ground for 30 minutes. Next, the mixed powders were thermally treated at 350 °C for 30 minutes with a heating rate of 5 °C/min under a reducing atmosphere. Finally, the calcined powders were washed with ultrapure water and alcohol to remove impurities until the pH of the suspension approached 7. TiO_{2-x} catalysts were then prepared by vacuum drying and grinding.

3. Preparation of PdCu NPs/TiO_{2-x} catalyst

In a typical synthesis, PdCu nano-particles (PdCu NPs) were prepared by a flexible co-

reduction method, and then PdCu NPs were loaded on TiO_{2-x} support by the solution impregnation method. First, a certain amount of $PdCl_2$ and $CuCl_2$ solution was dissolved in 50 mL of ultrapure water. Then 100 mg of PVP was added into the solution under magnetic stirring for 5 min, followed by the dropwise addition of $NaBH_4$ solution (150 mg of $NaBH_4$ dissolved in 15ml of ultrapure water) in 30 min. The mixed solution was magnetically stirred for 1 h, and then 100 mg of pre-prepared TiO_{2-x} powder was dispersed in the solution and magnetically stirred for 3 h. The samples were washed several times with ultrapure water and ethanol to eliminate the PVP and contaminants. The total amount of Pd^{2+} and Cu^{2+} was 6 mol% of TiO_2, and the obtained samples were denoted as Pd_1Cu_1 NPs/TiO_{2-x}, (Pd: Cu = 1: 1), Pd_1Cu_2 NPs/TiO_{2-x} and Pd_2Cu_1 NPs/TiO_{2-x} according to the amount of added $PdCl_2$ and $CuCl_2$. For comparison, Pd NPs, and Cu NPs were prepared and loaded on TiO_{2-x} support in the same manner.

4. Preparation of working electrodes

The working electrodes were prepared by loading the catalysts onto a 0.25 cm^2 hydrophobic carbon paper. First, the carbon paper (Incole Union Tianjin) was washed with ethanol several times. Then, a homogeneous mixture containing 5 mg of catalyst powder, 0.9 mL of isopropyl alcohol, and 0.1 mL of Nafion solution (5 wt%) was ultrasonically treated for 30 minutes. Working electrodes loaded with 0.1 mg/cm^2 catalyst were prepared by loading 5 μL of the mixture onto 0.5 × 0.5 cm^2 carbon papers.

5. Characterizations

SEM characterizations were conducted on a ZEISS GeminiSEM 300 scanning electron microscope. TEM, EDS and SAED characterizations were performed using an FEI Talos F200X G2 electron microscopy. XPS and AES characterizations were carried out using a

Thermo Scientific K-Alpha. XRD characterizations were performed using a PANalytical X'pert diffractometer. EPR data were collected from a Bruker E500. N_2 yield experiments were carried out using a GC9190 (equipped with a TCD and He as the carrier gas), while H_2 yield experiments were carried out using a GC7900 (equipped with a TCD and Ar as the carrier gas). In situ ATR-SEIRAS characterizations were carried out using a Bruker Tensor II with an MCT detector.

6. Electrochemical measurements

The yield experiments for electrochemical nitrate reduction were conducted using an electrochemical workstation (CS3104, CorrTest, Wuhan). Electrochemical characterizations were performed using a Zennium Pro electrochemical workstation. A Nafion 117 membrane was used to separate the anode and cathode of an H-type electrolytic cell employed in this work. Platinum foil and Ag/AgCl electrodes were used as the counter electrode and reference electrode, respectively. A mixed solution of 0.5 M Na_2SO_4 and 0.1 M $NaNO_3$ (total 30 ml) was used as both catholyte and anolyte. All potentials mentioned in this work were converted to RHE:

$$E_{RHE} = E_{Ag/AgCl} + 0.059 \times pH + 0.197$$

All the polarization curves were recorded after continuous cycles until they reached a steady state. The linear sweep voltammetry tests were performed at a rate of 100 mV/s. The cyclic voltammetry tests were performed at a rate of 5, 10, 20, 40, and 80 mV/s. The electrochemical impedance spectroscopy tests were performed at a frequency of 0.1-10^5 Hz and an amplitude of 5 mV. The nitrate reduction experiments were conducted at different potentials for 0.5 h at a stirring rate of ~400 rpm.

7. Determination of the rate of NH_3 and NO_2^- formation and FE

The ammonia formation rate was determined using the salicylic acid method. The salicylic acid method indicator was prepared by mixing three reagents: chromogenic reagent (A), oxidizing solution (B), and catalyzing reagent (C). To prepare the chromogenic reagent (A): 5 g salicylic acid ($C_7H_6O_3$) and 5 g sodium citrate tribasic dehydrate ($C_6H_9Na_3O_9$) were dissolved in 100 mL of 1 M NaOH. For the oxidizing solution (B), 3.5 mL of sodium hypochlorite (available chlorine 10-15%) was added to 100 mL of deionized water. To prepare the catalyzing reagent (C), 300 mg of sodium nitroferricyanide ($C_5FeN_6Na_2O$) was dissolved in 30 mL of deionized water. To measure the ammonia formation rate by UV-Vis absorbance, 2 mL of Chromogenic reagent (A), 1 mL of oxidizing solution (B) and 0.2 mL of catalyzing reagent (C) were added to 2 mL of electrolyte[1]. The absorption intensity at a wavelength of 655.5 nm was recorded after 2 h of developing time. The concentration-absorbance curve was calibrated using a series of standard ammonia chloride solutions, as shown in Figure S16.

A mixture of p-aminobenzenesulfonamide (4 g), N-(1-Naphthyl) ethylenediamine dihydrochloride (0.2 g), ultrapure water (50 mL) and phosphoric acid (10 mL, ρ=1.70 g/mL) was used as the chromogenic reagent to determine NO_2^-. A certain amount of electrolyte was taken out from the electrolytic cell and diluted to 5 mL to fall within the detection range. Next, 0.1 mL of the chromogenic reagent was added to the diluted solution and mixed thoroughly. After a 20-min developing time, the absorption intensity at a wavelength of 540 nm was recorded. The concentration-absorbance curve was calibrated using a series of standard sodium nitrite solutions (Figure S16).

The formation rate was determined using the following equation:

$$Yield\ rate = \frac{C \times V}{M \times t \times A}$$

The Faradaic efficiency (FE) was calculated as follows:

$$FE = \frac{n \times F \times C \times V}{M \times Q}$$

where C is the measured concentration of NH_3 or NO_2^-, V is the volume of the electrolyte (30 mL), M is the molar mass (17 for NH_3 and 46 for NO_2^-), t is the reaction time (0.5 h), A is the geometric area of the working electrode (0.25 cm^2), n is the transfer number of electron (8 for NH_3 and 2 for NO_2^-), F is Faraday constant (96485 C mol^{-1}), Q is the total charge used for the electrodes.

8. Determination of the rate of N_2 and H_2 formation and FE

To eliminate interference from the air, Ar was bubbled into the cathode chamber of an H-type electrolytic cell for 0.5h, then the cell was sealed (Figure S17). NITRR was carried out in the sealed H-type electrolytic cell at -1.4 V in a 0.5 M Na_2SO_4 + 0.1 M $NaNO_3$ electrolyte for 0.5 h. Then, 1 mL of gas in the cathode chamber was injected into a gas chromatograph (GC 9190, with TCD and He carrier gas) using a microsyringe for N_2 determination, and another 1 mL of gas in the cathode chamber was injected into another gas chromatograph (GC 7900, with TCD and Ar carrier gas) for H_2 determination. The concentration of N_2 and H_2 in the cathode chamber was calculated based on the characteristic peak area and calibration curves, as shown in Figure S19. The formation rate was determined using the following equation:

$$Yield\ rate = \frac{C \times V_{gas}}{V_m \times t \times A}$$

The Faradaic efficiency (FE) was calculated as follows:

$$FE = \frac{n \times F \times C \times V_{gas}}{V_m \times Q}$$

where C is the measured concentration of N_2 or H_2, V_{gas} is the volume of the gas in the cathode chamber (37 mL), V_m is the molar volume of gas (22.4 L/mol), t is the reaction time (0.5 h), A is the geometric area of the working electrode (0.25 cm^2), n is the transfer number of electron (10 for N_2 and 2 for H_2), F is Faraday constant (96485 C mol^{-1}), Q is the total charge used for the electrodes.

9. In situ attenuated total reflection surface-enhanced infrared absorption spectroscopy (ATR-SEIRAS) characterization

In situ ATR-SEIRAS spectra were collected using a BRUKER FTIR spectrometer (Tensor II with MCT detector) equipped with a homemade reaction cell (Figure S28). To enhance the infrared signals, a gold film was deposited onto the surface of a silicon crystal using chemical deposition. 50 μL of the prepared suspension of catalyst (TiO_{2-x} and PdCu NPs/TiO_{2-x}) was loaded on the glass carbon working electrode, while a platinum electrode and Ag/AgCl electrode served as the counter electrode and reference electrode, respectively. Different solution, including 0.5 M Na_2SO_4 + 0.1 M $NaNO_3$, 0.5 M Na_2SO_4 + 0.1 M $Na^{15}NO_3$, 0.5 M Na_2SO_4, 0.1 M $NaNO_3$, and ultrapure water were used as the electrolyte. The background spectra of the working electrode were recorded at an open circuit before each measurement.

10. DFT Calculations

Density functional theory (DFT) calculations were performed using Vienna ab initio

simulation package (VASP) with projector augmented wave (PAW) pseudopotential. The (101) surface of anatase TiO_2 was selected to study the effects of PdCu NPs loading on the catalytic activity of the NITRR. To investigate the interaction between PdCu NPs and oxygen vacancy, a structural model of PdCu NPs was placed next to the oxygen vacancy, and one oxygen atom of the anatase (101) TiO_2 structural model was removed for the simulation of oxygen vacancy. The Perdew−Burke−Ernzerhof (PBE) functional with the generalized gradient approximation (GGA) was used to describe the exchange-correlation energy in the calculations. Due to the strong correlation effect among the localized Ti *3d* electrons, the GGA+U method with an effective U value of 3.5 eV was used, consistent with previous work. The TiO_2 (101) model consisted of a (2×2) slab with four layers (O-Ti-O), and a vacuum layer of 15 Å in the z-direction was added to eliminate the longitudinal interlayer interaction. The cut-off energy of the plane-wave basis was set to 380 eV. The convergence threshold for the total energy and the force was set to 10^{-5} eV and 0.02 eV $Å^{-1}$, respectively. The maximum of calculation step was set to 2000, the minimum number of self-consistent step of the electron was set to 4, the scaling factor of the force was set to 0.2, and others was set to the default value. The Gibbs free energy change (ΔG) of each reduction step was calculated using $\Delta G = \Delta E + \Delta E_{ZPE} - T\Delta S$, where E, E_{ZPE}, and ΔS are the total energy, zero-point energy and entropy at 298 K from DFT calculations, respectively. The adsorption energy (E_{ad}) of each intermediate was calculated using $E_{ad} = E_{AB} - E_A - E_B$, where E_{AB}, E_A, and E_B are the total energy of the intermediate adsorbed on the catalyst, the total energy of the intermediate and the total energy of the catalyst, respectively. The partial Crystal Orbital Hamilton Population (COHP) spectra were calculated using Lobster 4.1.0 to analyze the bonding situations between selected atoms. Positive peaks in

the COHP spectra represent bonding molecular orbitals, and negative peaks represent antibonding molecular orbitals[2].

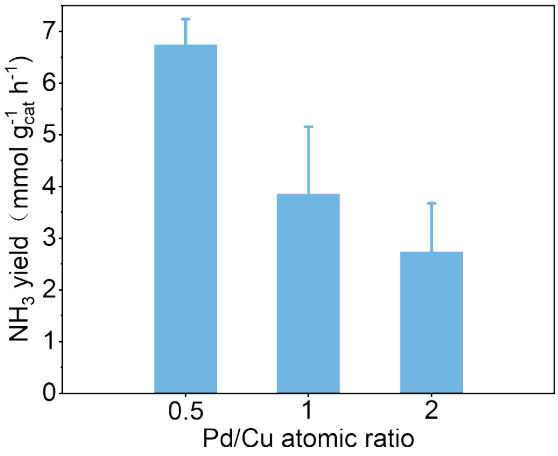

Figure S1. The NH_3 yield of NITRR (-0.8 V) varies with the Pd/Cu atomic ratio of PdCu/TiO_{2-x}.

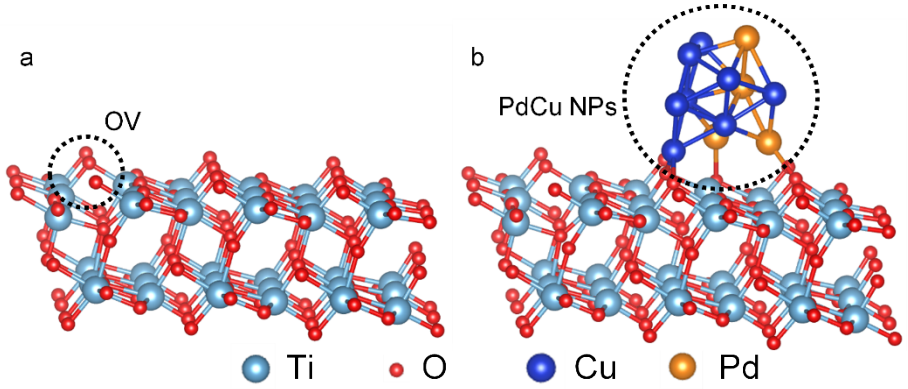

Figure S2. The structural model applicated in this work. The model of (a) TiO_{2-x}, (b) PdCu/TiO_{2-x}. The models are constructed based on the (101) main crystal plane of TiO_{2-x}, the presence of oxygen vacancy on the surface, the lattice constant of PdCu NPs, the appropriate simplification, and previous studies. [3,4]

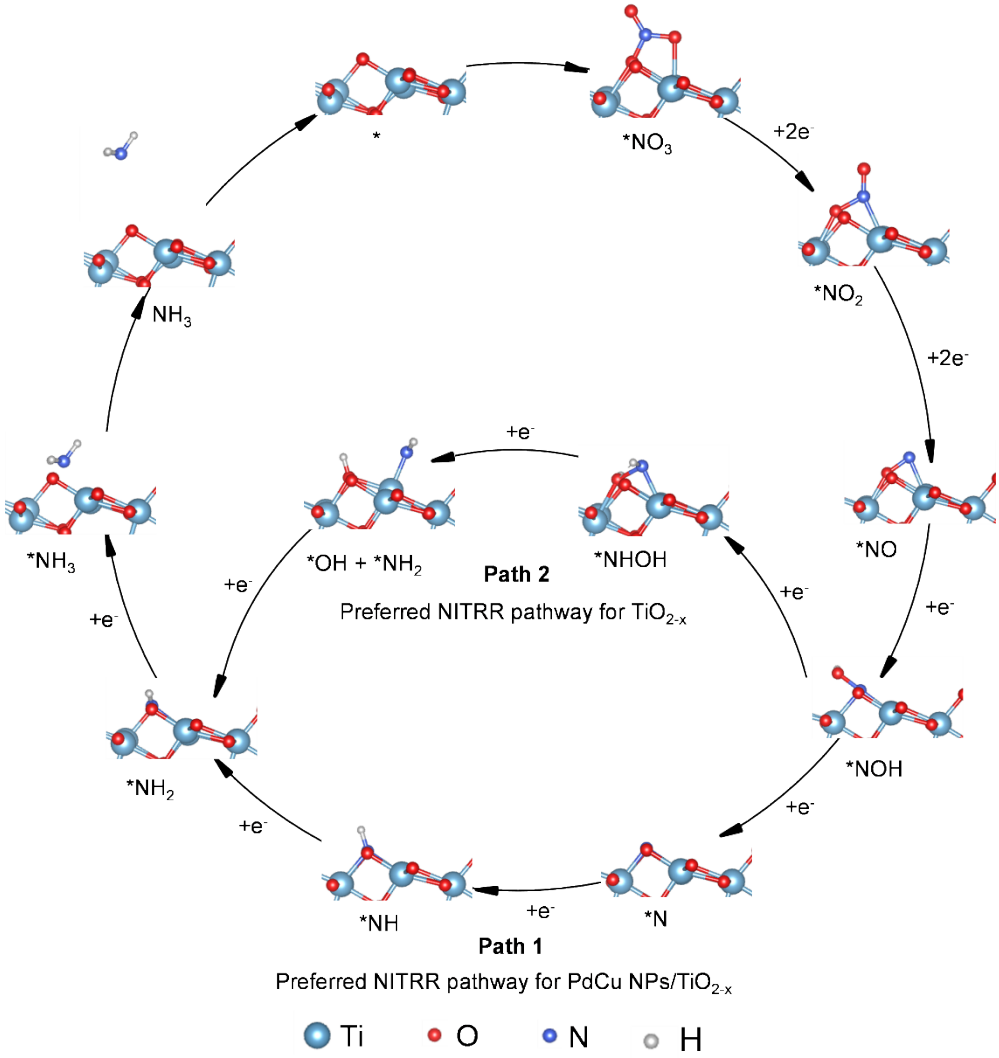

Figure S3. The structure model of the initial state of the reactive site, intermediate adsorbed states, and final product NH_3 of two reaction pathways.

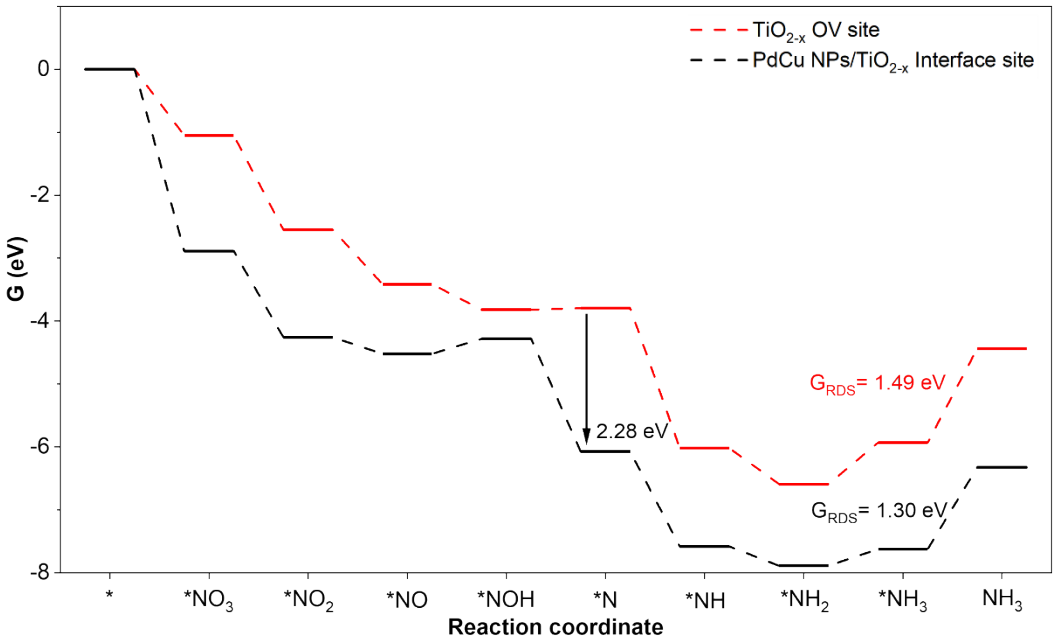

Figure S4. The Gibbs free energy of the NITRR rate-determining steps at different reaction sites.

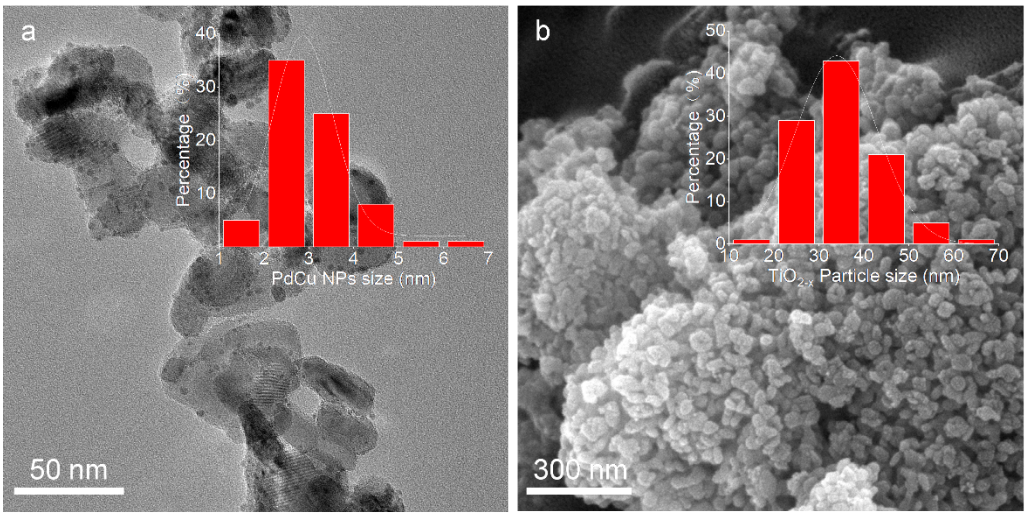

Figure S5. Microscopic morphology of PdCu NPs/TiO_{2-x} studied in this work. (a) The TEM image of PdCu NPs/TiO_{2-x} and size distribution of PdCu NPs on the TiO_{2-x} support, (b) The SEM image of PdCu NPs/TiO_{2-x} and size distribution of TiO_{2-x}.

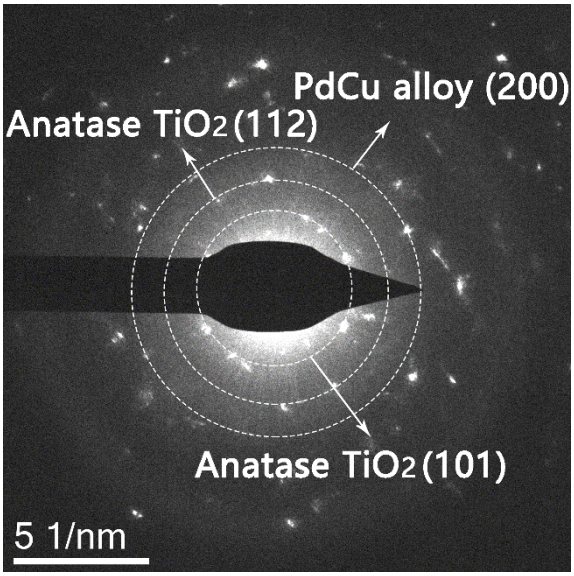

Figure S6. SAED image of PdCu NPs/TiO_{2-x}, the area in Figure S5(a) is the selected area.

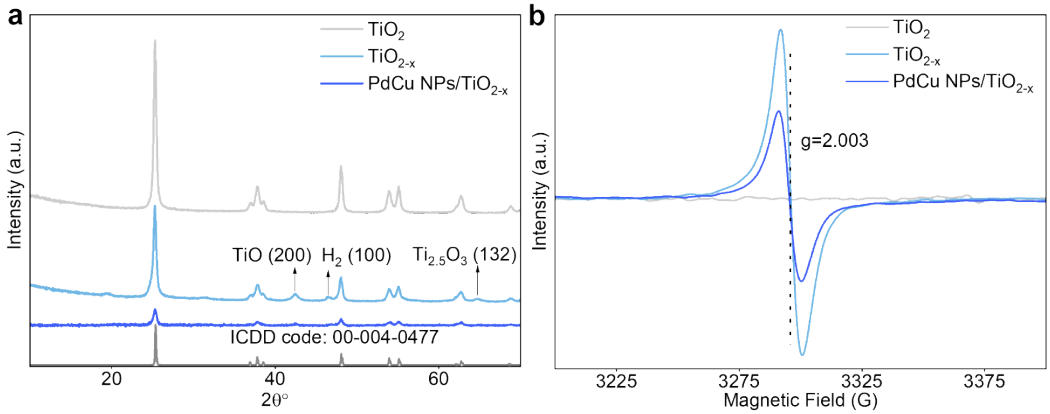

Figure S7. The XRD pattern (a) and EPR pattern (b) of TiO_2, TiO_{2-x} and PdCu NPs/TiO_{2-x}. The diffraction pattern for TiO_{2-x} possesses three additional peaks at 42.4°, 46.5°, and 64.6°, corresponding to (200) of TiO (ICDD 00-002-1196), (100) of H_2 (ICDD 01-085-1647), and (132) of $Ti_{2.5}O_3$ (ICDD 03-065-6711), respectively. These trace impurities result from the reduction of TiO_2 using $NaBH_4$.

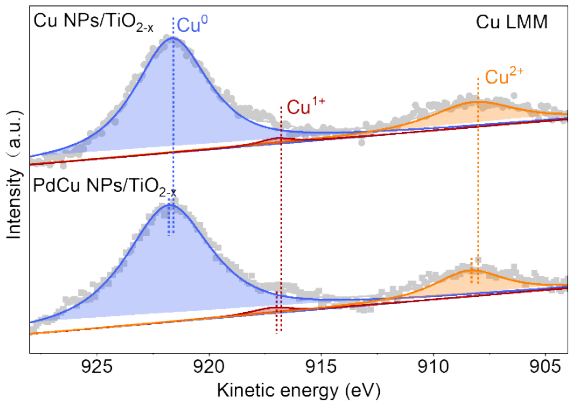

Figure S8. The Cu LMM AES pattern of Cu NPs/TiO_{2-x} and PdCu NPs/TiO_{2-x}. The peak area ratio for

Cu^{1+} increases from 2.4% to 2.7% with the introduction of Pd. The peak area ratio for Cu^{2+} decreases from 13.4% to 13.1% with the introduction of Pd.

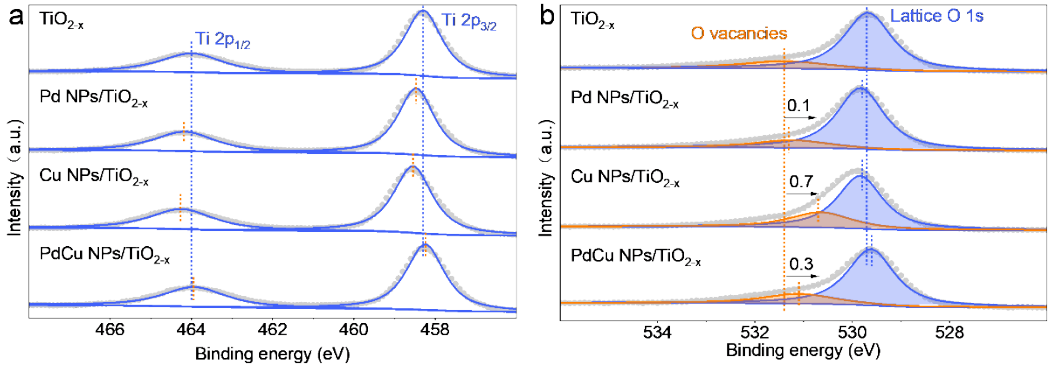

Figure S9. The XPS spectra for Ti 2p (a) and O 1s (b) of TiO_{2-x}, Pd NPs/TiO_{2-x}, Cu NPs/TiO_{2-x} and PdCu NPs/TiO_{2-x}. The peak area ratios for O vacancies are 19.5%, 17.2%, 29.0%, and 22.6% in TiO_{2-x}, Pd NPs/TiO_{2-x}, Cu NPs/TiO_{2-x}, and PdCu NPs/TiO_{2-x}, respectively.

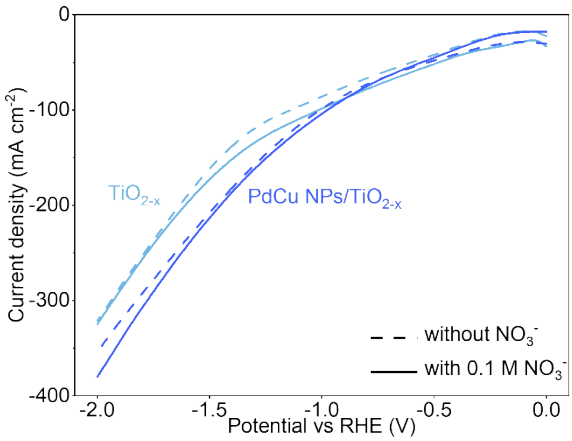

Figure S10. The LSV curves of TiO_{2-x} and PdCu NPs/TiO_{2-x} in electrolyte with or without 0.1 M NO_3^-.

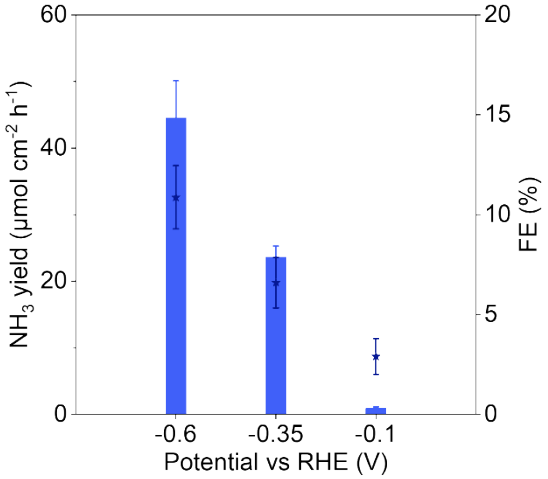

Figure S11. The NH_3 yield rate and faradaic efficiency over PdCu NPs/TiO_{2-x} at given potentials.

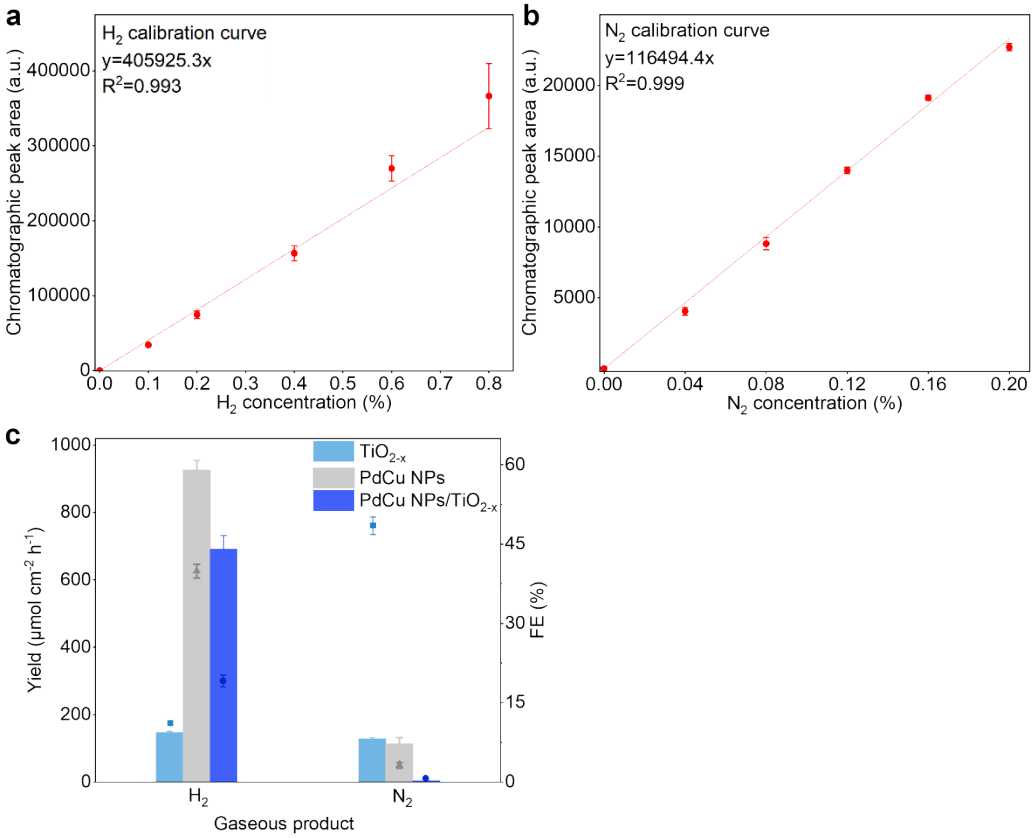

Figure S12. The calibration curves of (a) H_2 and (b) N_2, the external standard method is applicated based on the sealed H-type electrolytic cell (Figure S13). (c) The yield rate of H_2 and N_2 of TiO_{2-x}, PdCu NPs and PdCu NPs/TiO_{2-x} at -1.4 V.

Figure S13. The sealed H-type electrolytic cell is used for the determination of gaseous products.

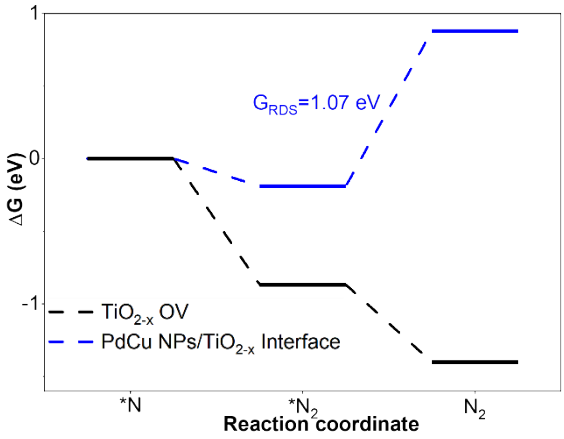

Figure S14. The DFT simulation of the N_2 formation process on TiO_{2-x} OV sites and PdCu NPs/TiO_{2-x} interface sites.

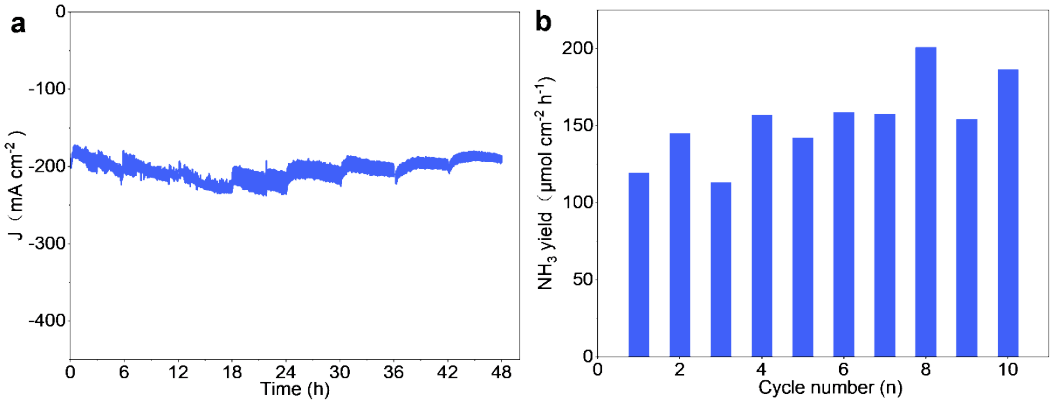

Figure S15. (a) The current density of PdCu NPs/TiO_{2-x} during 48h NITRR process at -1.4 V. (b) The NH_3 yield rate over PdCu NPs/TiO_{2-x} after consecutive cycling test at -1.4 V.

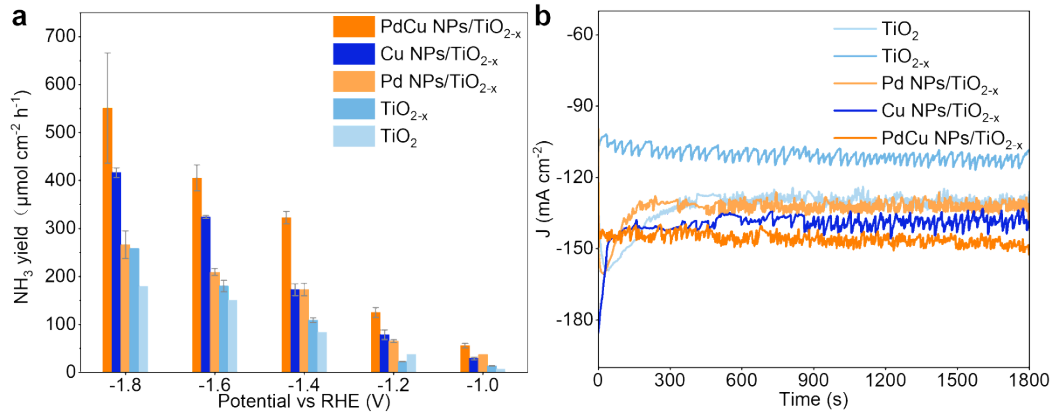

Figure S16. (a) The NH_3 yield rate comparison of TiO_2, TiO_{2-x}, Pd NPs/TiO_{2-x}, Cu NPs/TiO_{2-x}, and PdCu NPs/TiO_{2-x} at given potentials. (b) The current density comparison of TiO_2, TiO_{2-x}, Pd NPs/TiO_{2-x}, Cu NPs/TiO_{2-x}, and PdCu NPs/TiO_{2-x} at -1.4 V.

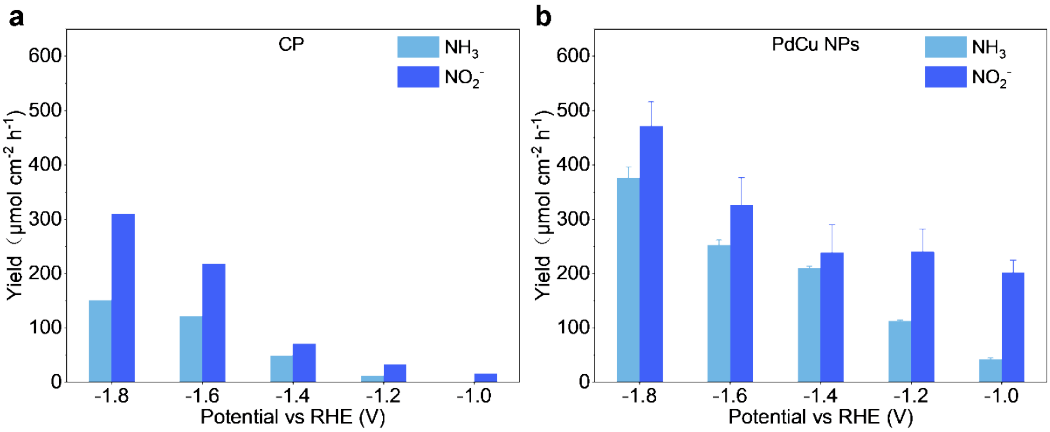

Figure S17. The comparison of NH_3 and NO_2^- yield rate over (a) carbon paper (CP), and (b) PdCu NPs loaded on CP.

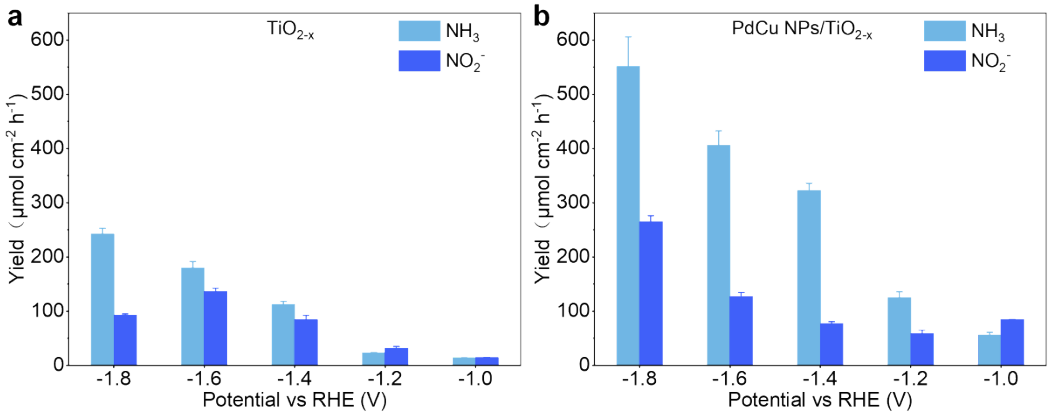

Figure S18. The comparison of NH_3 and NO_2^- yield rate over (a) TiO_{2-x}, and (b) PdCu NPs/TiO_{2-x}.

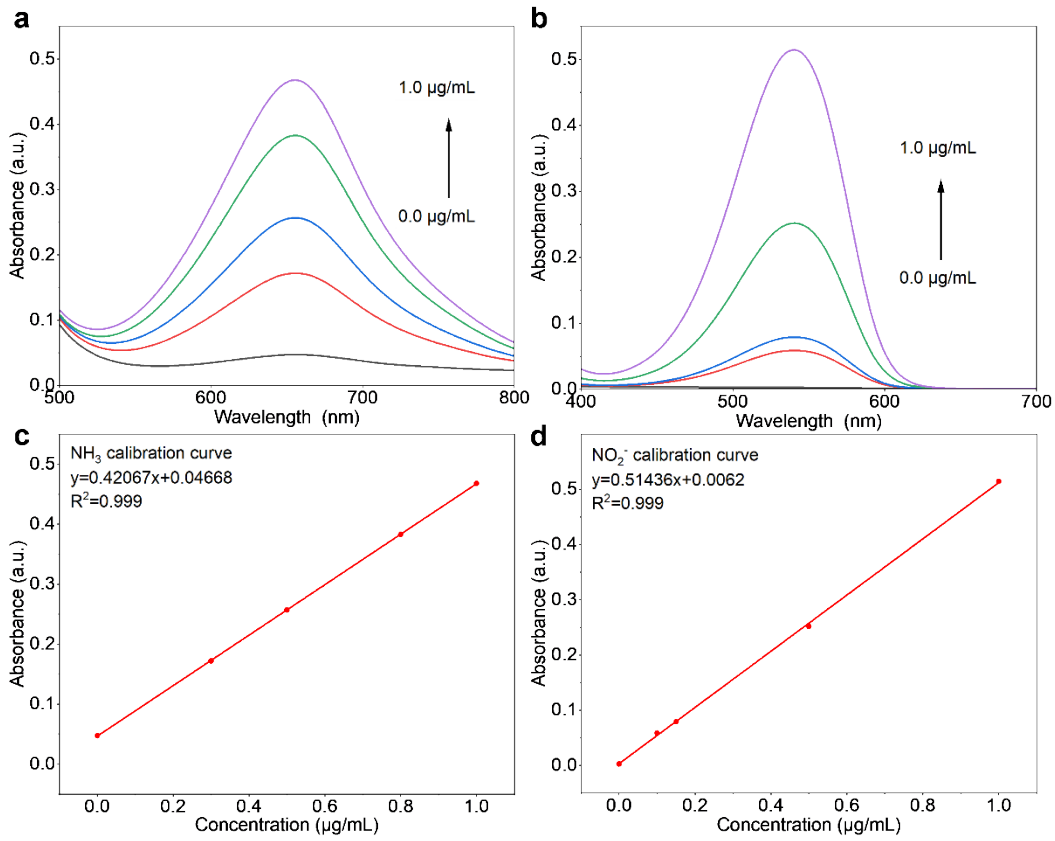

Figure S19. The calibration curves in 0.5 M Na_2SO_4 using NH_4Cl and $NaNO_2$ solutions of known concentrations as the standards. UV-vis curves for (a) NH_3 and (b) NO_2^-. Calibration curves were used to determine the (c) NH_3 and (d) NO_2^- concentration.

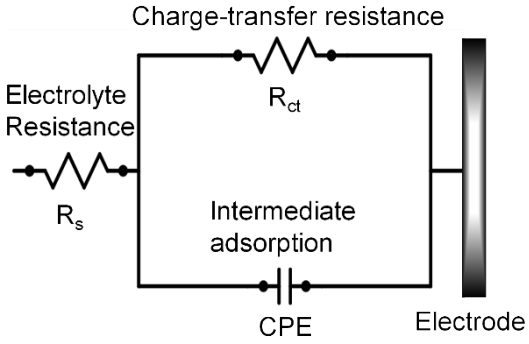

Figure S20. The equivalent circuit model is used in the fitting of the impedance data. The constant phase element (CPE) is the model of charge storage via adsorption/desorption of *H and *NO_3 intermediates at the surface of the electrode[5]. In contrast with the equivalent circuit model, which contains two CPE, used in the previous study, the model used in this study only contains one CPE, since the charge-storage via intercalation/de-intercalation of electrolyte ions at the interior region of the electrode is negligible for CP electrode[6].

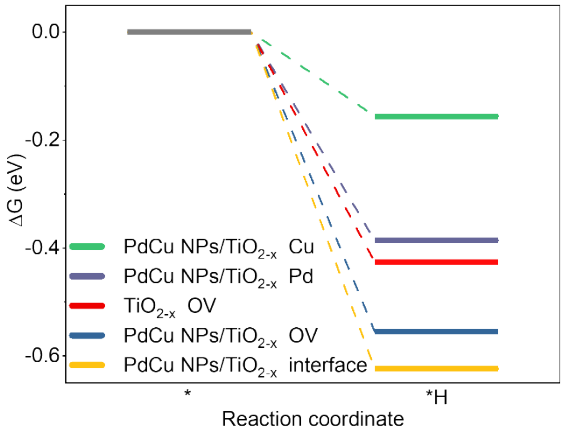

Figure S21. The ΔG of *H intermediate at different sites: Cu, Pd, OV and interface sites of PdCu NPs/TiO_{2-x} and OV site of TiO_{2-x}.

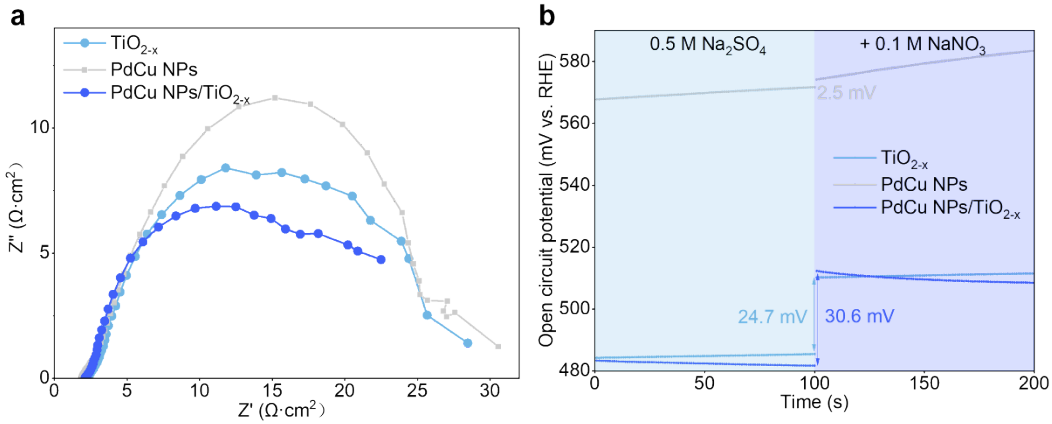

Figure S22. The (a) unfitted Nyquist plots for TiO_{2-x}, PdCu NPs and PdCu NPs/TiO_{2-x}, and (b) the OCP curves of TiO_{2-x}, PdCu NPs and PdCu NPs/TiO_{2-x} in 0.5 M Na_2SO_4, and 0.1 M $NaNO_3$ was injected subsequently.

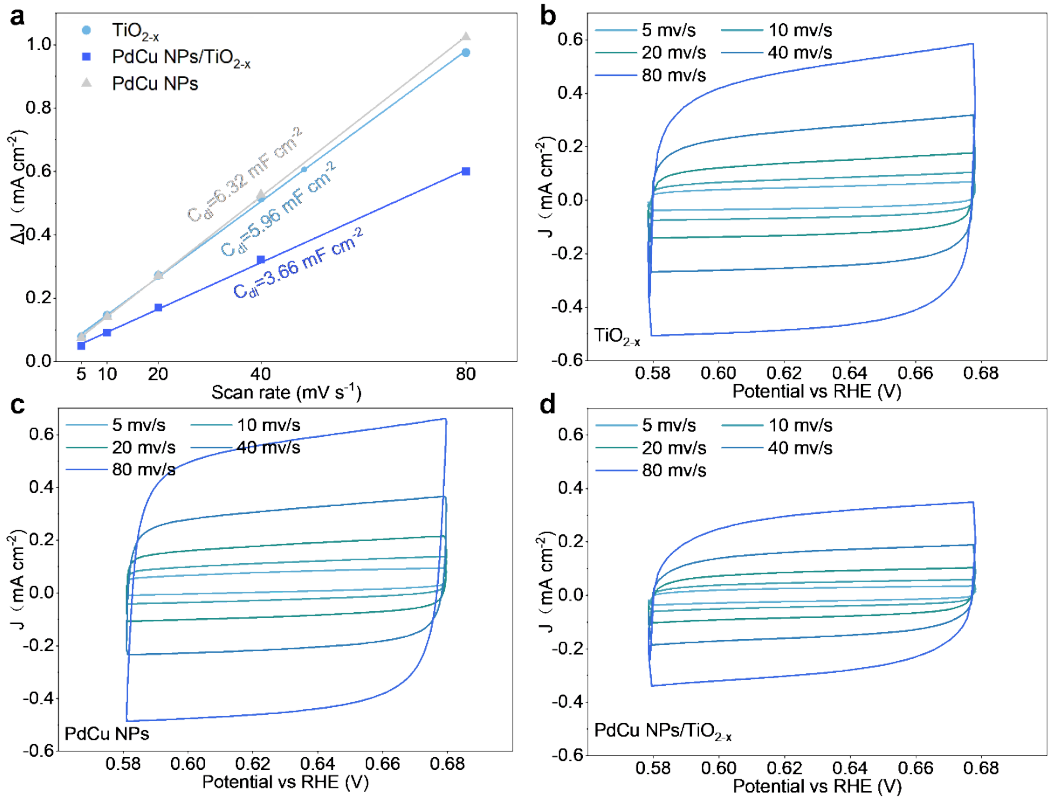

Figure S23. The (a) electrochemically active surface area. The CV curves of (b) TiO_{2-x}, (c) PdCu NPs and (d) PdCu NPs/TiO_{2-x}.

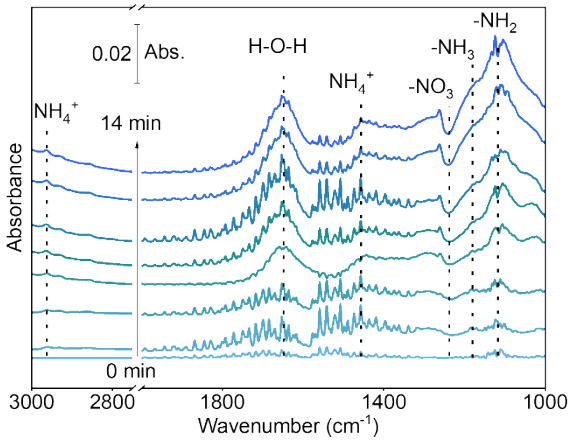

Figure S24. Time-resolved in situ electrochemical ATR-SEIRAS spectra over PdCu NPs/TiO_{2-x} at −1.0 V in 0.1 M $NaNO_3$ electrolyte.

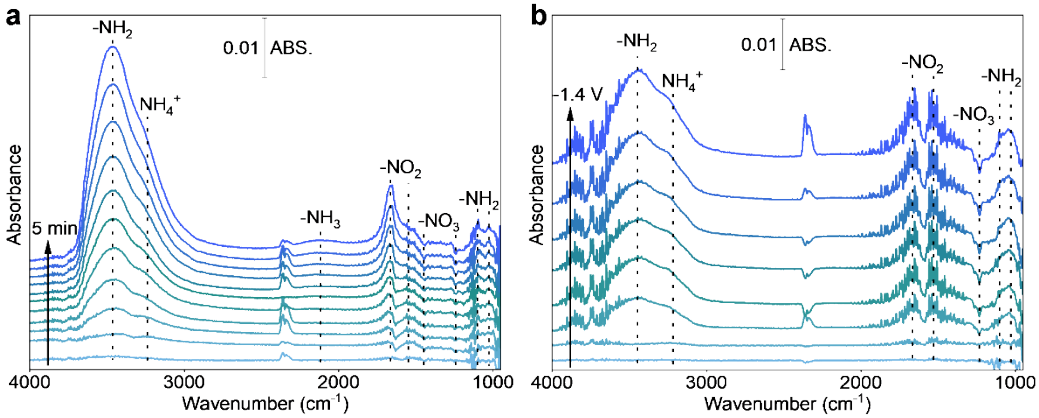

Figure S25. (a) Time-resolved in situ electrochemical ATR-SEIRAS spectra over PdCu NPs/TiO_{2-x} at −1.4 V, and (b) potential-resolved in situ electrochemical ATR-SEIRAS spectra over PdCu NPs/TiO_{2-x} (30s reaction time at each potential, step: -0.2 V) in 0.5 M Na_2SO_4 supporting electrolyte with isotopically labelled 0.1 M $Na^{15}NO_3$ electrolyte.

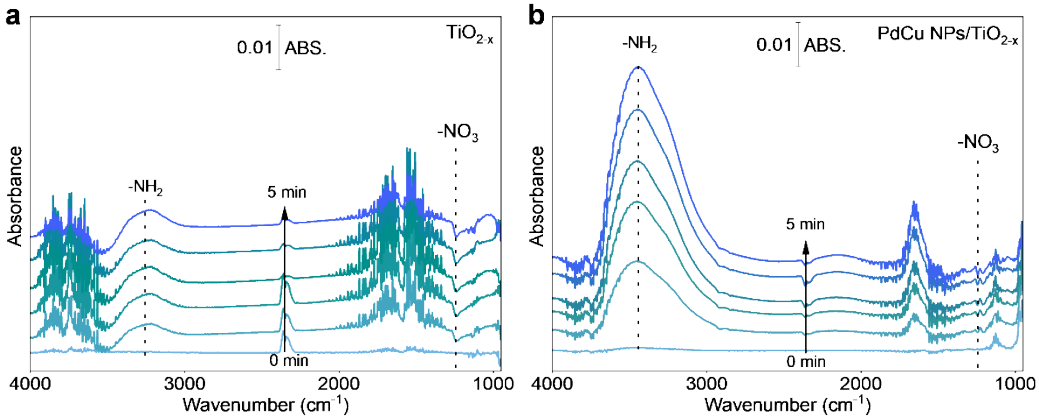

Figure S26. Time-resolved in situ electrochemical ATR-SEIRAS spectra over (a) TiO_{2-x}, and (b) PdCu NPs/TiO_{2-x} at −1.8 V vs RHE in 0.1 M $NaNO_3$ electrolyte.

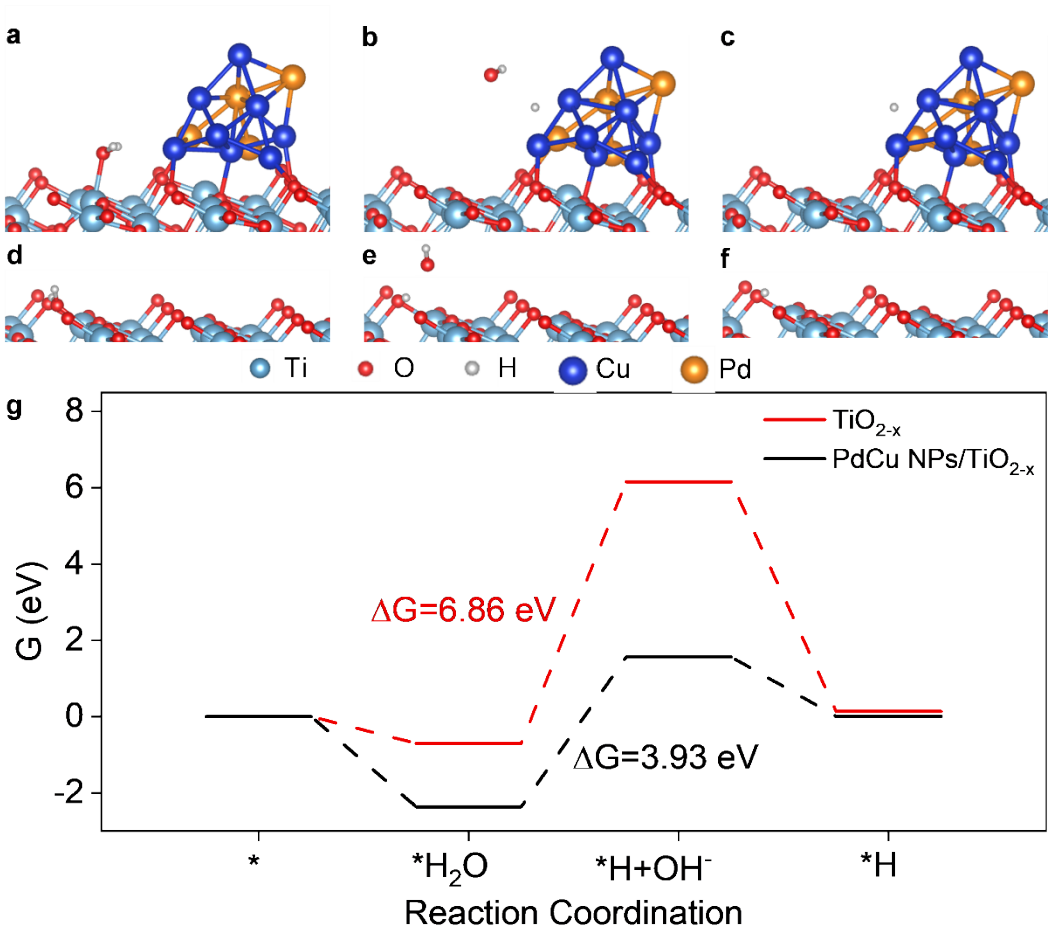

Figure S27. The simulated model of *H_2O adsorption, dissociation and *H adsorption on the surface of (a - c) PdCu NPs/TiO_{2-x} and (d - f) TiO_{2-x}, respectively. (g) The ΔG of the *H produce process.

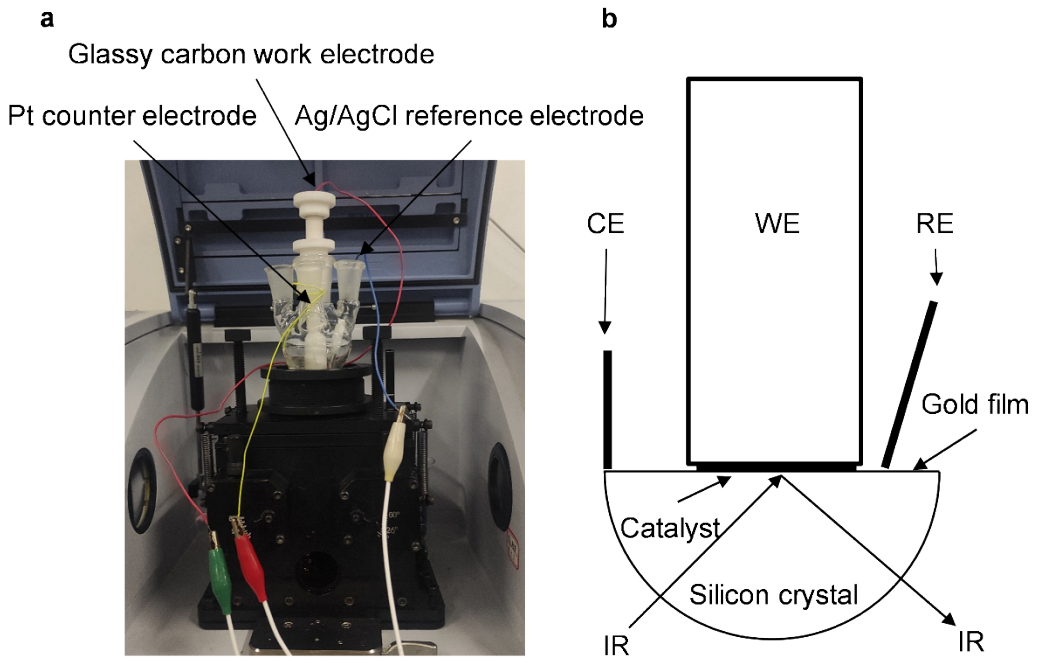

Figure S28. (a) The electrochemical in situ IR spectroscopy equipment used in this work, and (b) the

schematic diagram of the equipment structure.

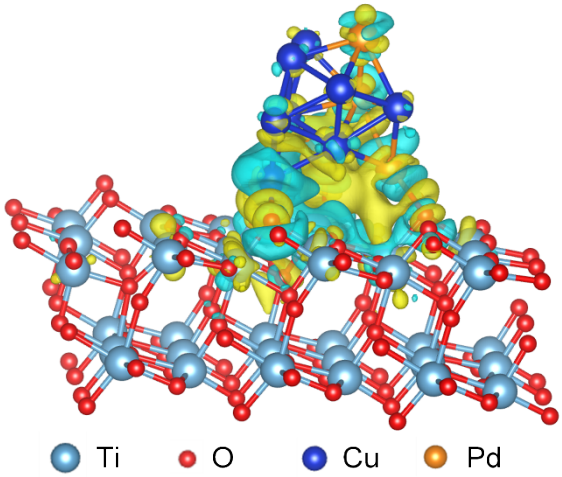

Figure S29. The differential charge density map of PdCu NPs/TiO_{2-x}. The green areas express electron depletion and the yellow areas refer to electron accumulation with an isosurface value of 0.001 electrons/Å^3.

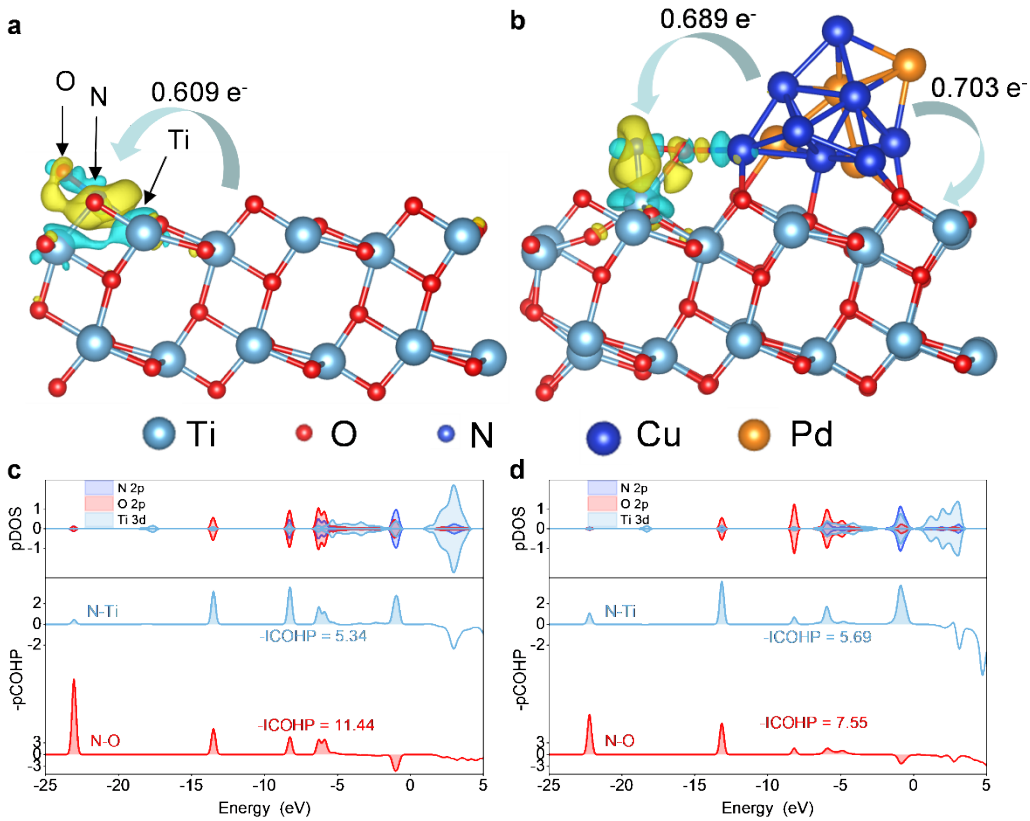

Figure S30. The differential charge density map and electron transfer between PdCu NPs, TiO_{2-x}, and *NOH intermediate adsorbed at (a) TiO_{2-x} OV, and (b) PdCu NPs/TiO_{2-x} interface, respectively. The PDOS and COHP of *NOH intermediate adsorbed at (c) TiO_{2-x} OV, and (d) PdCu NPs/TiO_{2-x} interface (The green areas express electron depletion and the yellow areas refer to electron accumulation with an isosurface value of 0.005 electrons/Å^3).

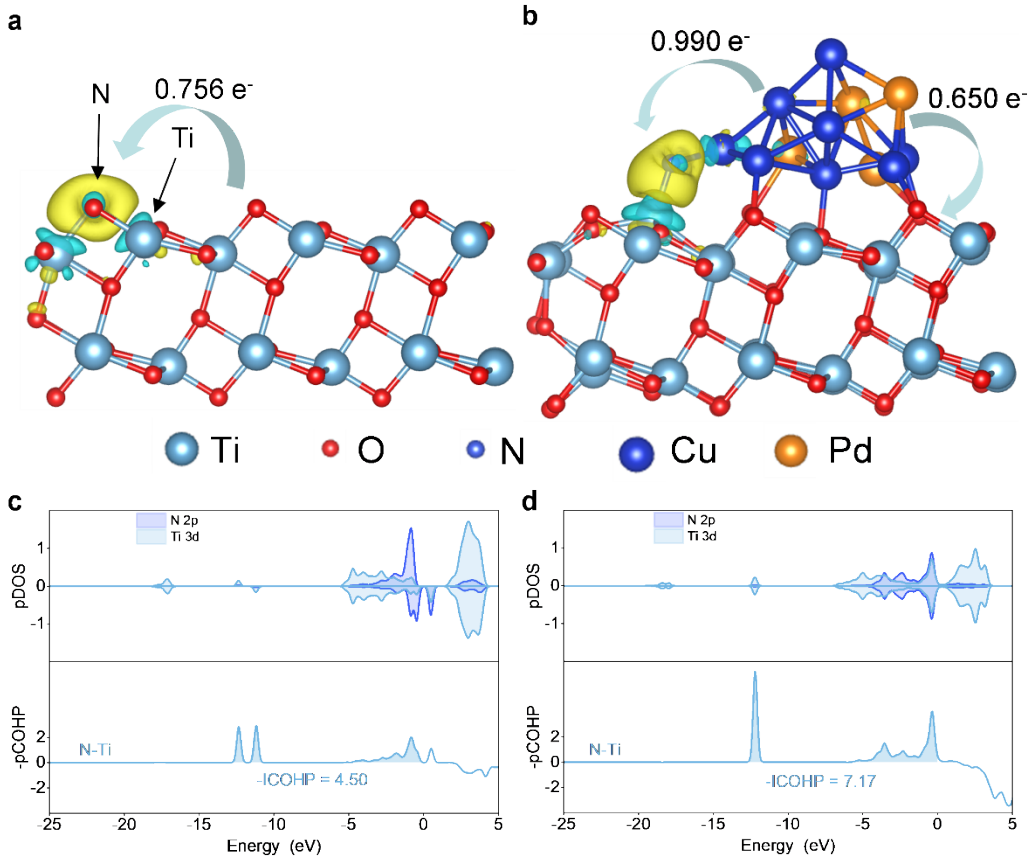

Figure S31. The differential charge density map and electron transfer between PdCu NPs, TiO_{2-x}, and *N intermediate adsorbed at (a) TiO_{2-x} OV, and (b) PdCu NPs/TiO_{2-x} interface, respectively. The PDOS and COHP of *N intermediate adsorbed at (c) TiO_{2-x} OV, and (d) PdCu NPs/TiO_{2-x} interface (The green areas express electron depletion and the yellow areas refer to electron accumulation with an isosurface value of 0.005 electrons/Å^3).

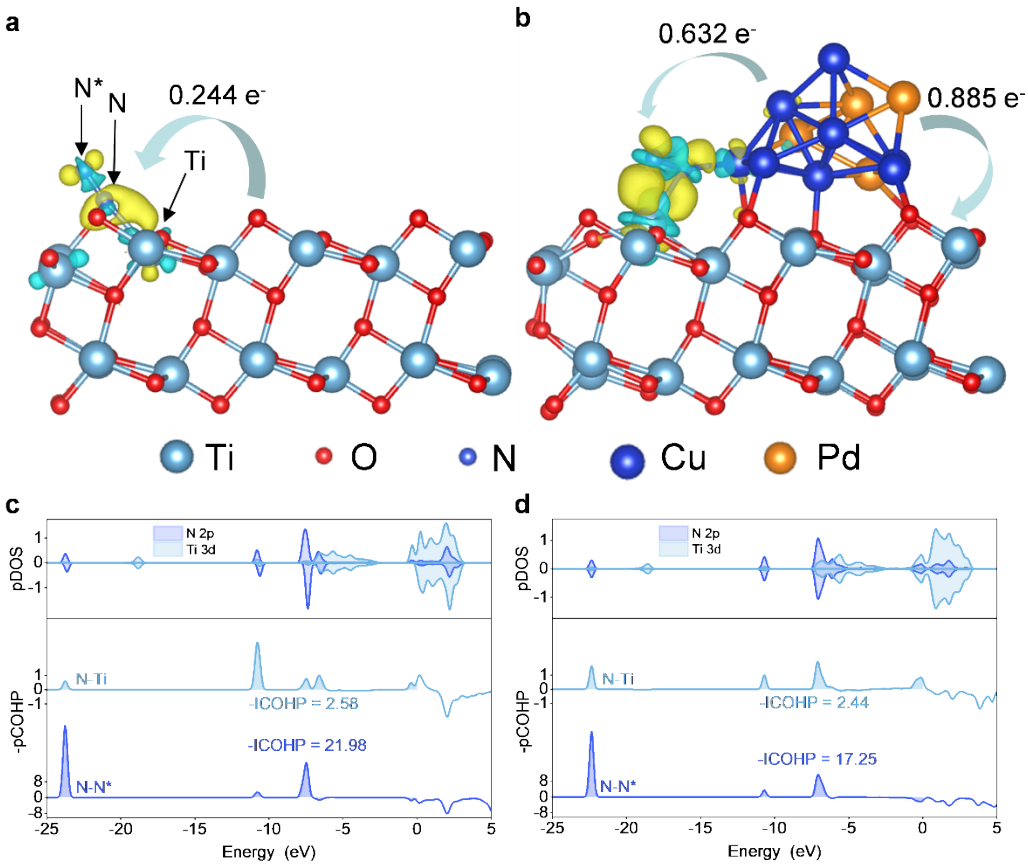

Figure S32. The differential charge density map and electron transfer between PdCu NPs, TiO_{2-x}, and $*N_2$ intermediate adsorbed at (a) TiO_{2-x} OV, and (b) PdCu NPs/TiO_{2-x} interface, respectively. The PDOS and COHP of $*N_2$ intermediate adsorbed at (c) TiO_{2-x} OV, and (d) PdCu NPs/TiO_{2-x} interface (The green areas express electron depletion and the yellow areas refer to electron accumulation with an isosurface value of 0.005 electrons/Å^3).

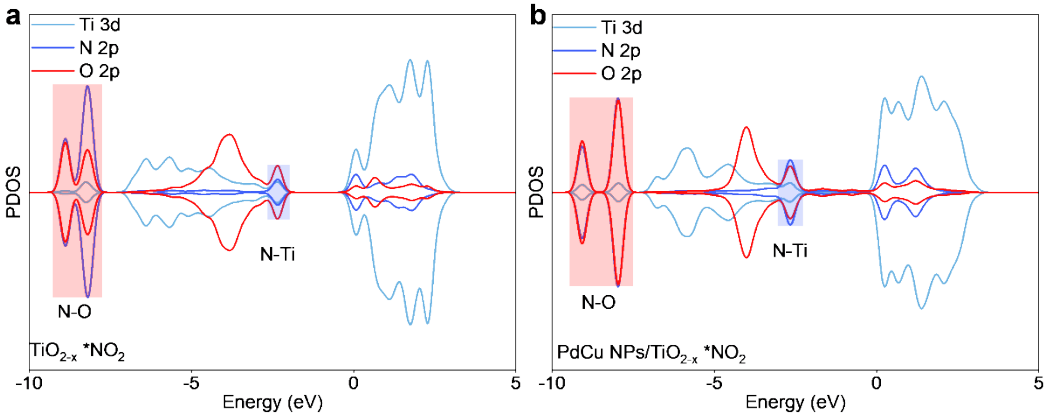

Figure S33. The PDOS of $*NO_2$ intermediate adsorbed at (a) TiO_{2-x} OV, and (b) PdCu NPs/TiO_{2-x} interface.

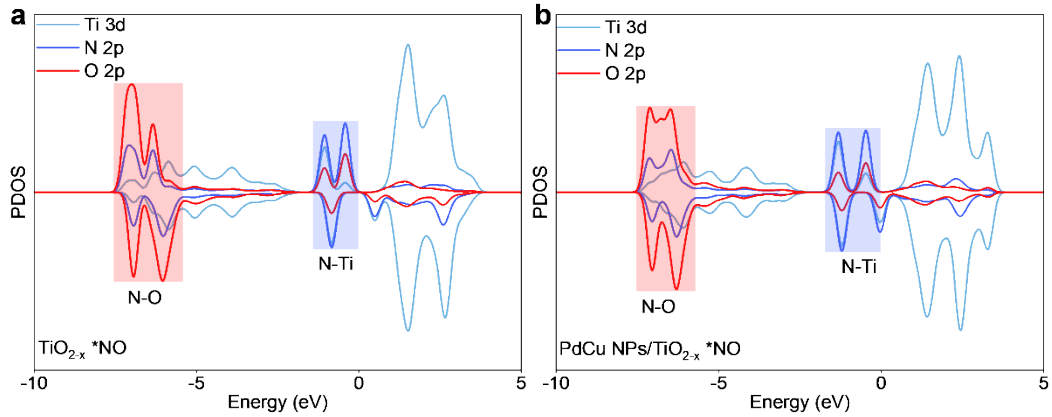

Figure S34. The PDOS of *NO intermediate adsorbed at (a) TiO_{2-x} OV, and (b) PdCu NPs/TiO_{2-x} interface.

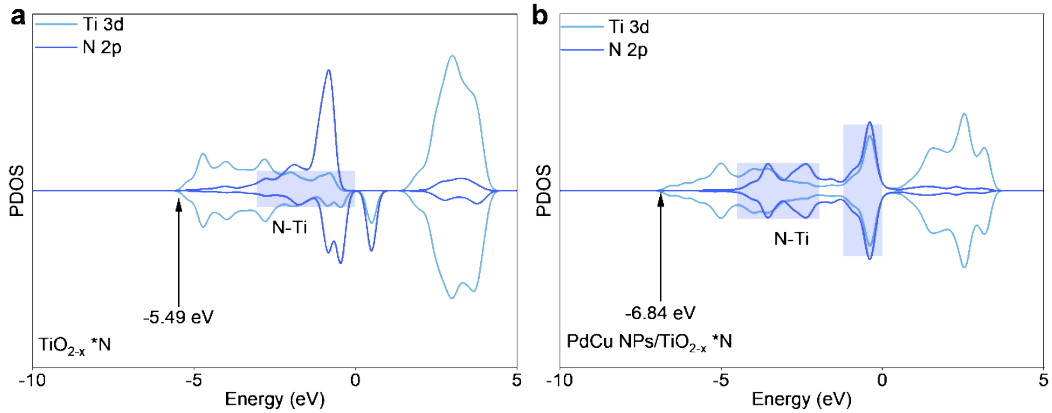

Figure S35. The PDOS of *N intermediate adsorbed at (a) TiO_{2-x} OV, and (b) PdCu NPs/TiO_{2-x} interface.

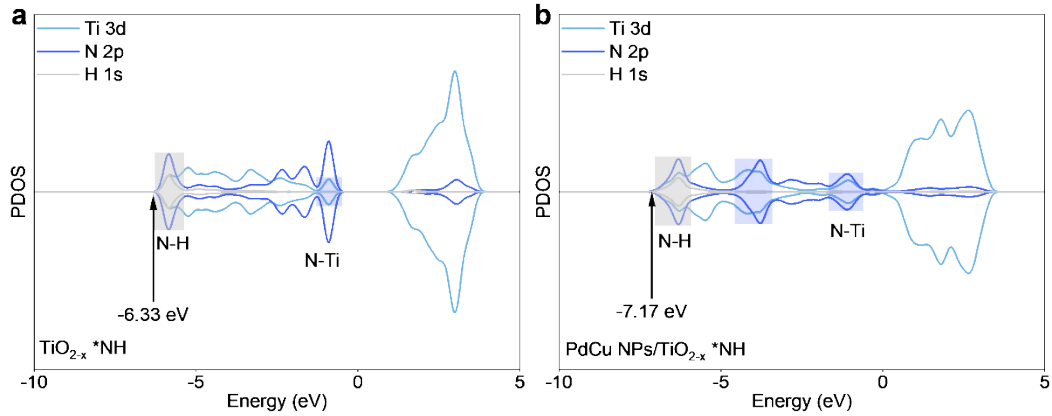

Figure S36. The PDOS of *NH intermediate adsorbed at (a) TiO_{2-x} OV, and (b) PdCu NPs/TiO_{2-x} interface.

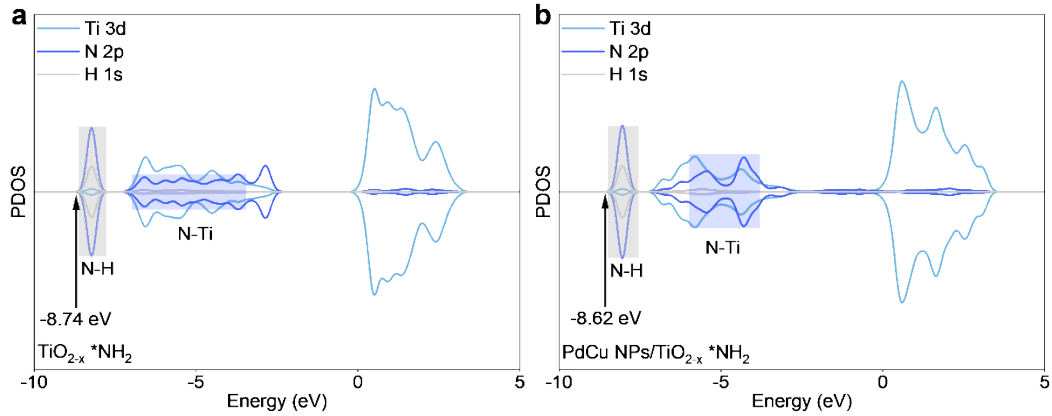

Figure S37. The PDOS of *NH_2 intermediate adsorbed at (a) TiO_{2-x} OV, and (b) PdCu NPs/TiO_{2-x} interface.

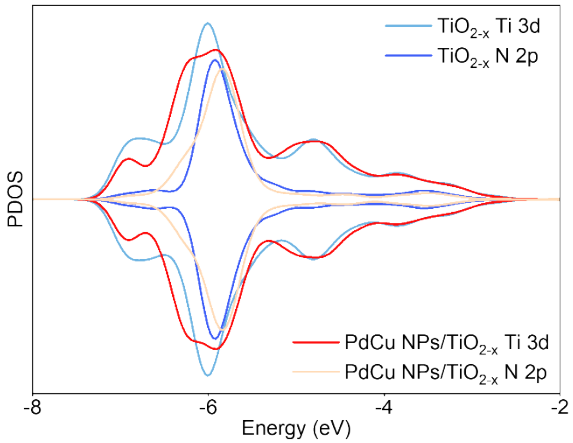

Figure S38. The PDOS of *NH_3 intermediate adsorbed at TiO_{2-x} OV and PdCu NPs/TiO_{2-x} interface.

Table S1. Reported activities for the electrocatalytic NRR on the PdCu-loaded catalysts.

Catalyst	Potential vs RHE	NH_3 yield	References
$Pd_{0.2}Cu_{0.8}$/rGO	-0.2 V	$2.80\ \mu g\ h^{-1} mg_{cat.}^{-1}$	7
PdCu/B	-0.4 V	$26.6\ \mu g\ h^{-1} mg_{cat.}^{-1}$	8
BCC PdCu NPs/C	-0.1 V	$35.7\ \mu g\ h^{-1} mg_{cat.}^{-1}$	9
Pd_3Cu_1 NPs/C	-0.25 V	$39.9\ \mu g\ h^{-1} mg_{cat.}^{-1}$	10
BCC OVs-PdCu NPs/C	0 V	$55.54\ \mu g\ h^{-1} mg_{cat.}^{-1}$	11
PdCu/NC	-0.45 V	$69.2\ \mu g\ h^{-1} mg_{cat.}^{-1}$	12
PdCu/TiO_{2-x}	-0.1 V	$144.7\ \mu g\ h^{-1} mg_{cat.}^{-1}$	13
PdCu/TiO_{2-x}	-0.3 V	$85\ \mu g\ h^{-1} mg_{cat.}^{-1}$	previous work

Table S2. The adsorption energy (E_{ad}) of *NO_3 at the six possible NITRR active sites.

Adsorption site	I	II	III	IV	V	VI
E_{ad} (eV)	-4.52	-4.57	-4.54	-4.43	-2.36	-2.88

Table S3. The E_{ad} of various intermediates at different sites.

	*NO_3	*NO_2	*NO	*NOH	*N	*NH	*NH_2	*NH_3	*N_2	*NHOH	*NH_2+*OH
TiO_{2-x}	-4.52	-4.21	-3.95	-5.19	-5.51	-6.59	-4.92	-1.73	-0.91	-3.83	-9.44
PdCu NPs	-4.54	-4.47	-3.55	-4.34	-6.43	-6.15	-4.67	-1.71	-1.61	-3.68	-9.69
TiO_{2-x}											

Table S4. The compositional distributions of Pd, Cu, Ti, and O at the EDS mapping surface.

Element	Atomic Fraction (%)	Mass Fraction (%)	Fit error (%)
Pd	0.45± 0.05	2.08± 0.27	0.68
Cu	2.08± 0.3	5.8± 0.86	0.18
Ti	16.99± 2.39	35.66± 3.9	0.04
O	80.48± 2.33	56.46± 3.45	1.33

Table S5. The ICP-MS results of PdCu NPs/TiO_{2-x}.

Element	Weight percentage (%)	Molar percentage relative to Ti (%)
Pd	2.58	2.57
Cu	3.03	5.05
Ti	45.27	100

Reference:

1 D. Yao, C. Tang, L. Li, B. Xia, A. Vasileff, H. Jin, Y. Zhang and S. Qiao, *Adv. Energy Mater.*, 2020, **10**, 2001289.

2 S. Steinberg and R. Dronskowski, *Crystals*, 2018, **8**, 225.

3 J. Li, R. Chen, J. Wang, Y. Zhou, G. Yang and F. Dong, *Nat. Commun.*, 2022, **13**, 1098.

4 Y. Jiang, M. Duchamp, S. J. Ang, H. Yan, T. L. Tan and U. Mirsaidov, *Nat. Commun.*, 2023, **14**, 104.

5 R. Ge, Y. Wang, Z. Li, M. Xu, S. Xu, H. Zhou, K. Ji, F. Chen, J. Zhou and H. Duan, *Angew. Chem. Int. Ed. Engl.*, 2022, **61**, e202200211.

6 S. Manoharan, S. Sahoo, P. Pazhamalai and S. J. Kim, *Int. J. Hydrogen Energy*, 2018, **43**, 1667–1674.

7 M.-M. Shi, D. Bao, S.-J. Li, B.-R. Wulan, J.-M. Yan and Q. Jiang, *Adv. Energy Mater.*, 2018, **8**, 1800124.

8 X. Zhang, Y. Cao, Z. F. Huang, S. Zhang, C. Liu, L. Pan, C. Shi, X. Zhang, Y. Zhou, G. Yang and J. J. Zou, *Carbon Energy*, 2023, **5**, e266.

9 W. Tong, B. Huang, P. Wang, L. Li, Q. Shao and X. Huang, *Angew. Chem. Int. Ed. Engl.*, 2020, **59**, 2649–2653.

10 F. Pang, Z. Wang, K. Zhang, J. He, W. Zhang, C. Guo and Y. Ding, *Nano Energy*, 2019, **58**, 834–841.

11 Z. Wang, X. Wu, J. Liu, D. Zhang, H. Zhao, X. Zhang, Y. Qin, N. Nie, D. Wang, J. Lai and L. Wang, *Nano Lett.*, 2021, **21**, 9580–9586.

12 L. Han, Z. Ren, P. Ou, H. Cheng, N. Rui, L. Lin, X. Liu, L. Zhuo, J. Song, J. Sun, J. Luo and H. L. Xin, *Angew. Chemie*, 2021, **133**, 349–354.

13 C. Liu, X. Guo, Z.-F. Huang, J. Li, L. Gan, L. Pan, C. Shi, X. Zhang, G. Yang and J.-J. Zou, *Mater. Chem. Front.*, 2022, **6**, 2190–2200.